

Article

Thermal Modelling and Temperature Estimation of a Cylindrical Lithium Iron Phosphate Cell Subjected to an Automotive Duty Cycle

Simha Sreekar Achanta , Abbas Fotouhi * , Hanwen Zhang  and Daniel J. Auger 

Faculty of Engineering and Applied Sciences, Cranfield University, Cranfield MK43 0AL, UK; simhasreekar.achanta.106@cranfield.ac.uk (S.S.A.); hanwen.zhang@cranfield.ac.uk (H.Z.); d.j.auger@cranfield.ac.uk (D.J.A.)

* Correspondence: a.fotouhi@cranfield.ac.uk; Tel.: +44-(0)1-2347-58092

Abstract: Li ion batteries are emerging as the mainstream source for propulsion in the automotive industry. Subjecting a battery to extreme conditions of charging and discharging can negatively impact its performance and reduce its cycle life. Assessing a battery's electrical and thermal behaviour is critical in the later stages of developing battery management systems (BMSs). The present study aims at the thermal modelling of a 3.3 Ah cylindrical 26650 lithium iron phosphate cell using ANSYS 2024 R1 software. The modelling phase involves iterating two geometries of the cell design to evaluate the cell's surface temperature. The multi-scale multi-domain solution method, coupled with the equivalent circuit model (ECM) solver, is used to determine the temperature characteristics of the cell. Area-weighted average values of the temperature are obtained using a homogeneous and isotropic assembly. A differential equation is implemented to estimate the temperature due to the electrochemical reactions and potential differences. During the discharge tests, the cell is subjected to a load current emulating the Worldwide Harmonised Light Vehicles Test Procedure (WLTP). The results from the finite element model indicate strikingly similar trends in temperature variations to the ones obtained from the experimental tests.



Academic Editors: Torsten Brezesinski and Zhenbo Wang

Received: 21 October 2024

Revised: 10 March 2025

Accepted: 18 March 2025

Published: 22 March 2025

Citation: Achanta, S.S.; Fotouhi, A.; Zhang, H.; Auger, D.J. Thermal Modelling and Temperature Estimation of a Cylindrical Lithium Iron Phosphate Cell Subjected to an Automotive Duty Cycle. *Batteries* **2025**, *11*, 119. <https://doi.org/10.3390/batteries11040119>

Copyright: © 2025 by the authors. Licensee MDPI, Basel, Switzerland. This article is an open access article distributed under the terms and conditions of the Creative Commons Attribution (CC BY) license (<https://creativecommons.org/licenses/by/4.0/>).

Keywords: lithium iron phosphate cell (LFP); temperature estimation; ANSYS; multi-scale multi-domain (MSMD); equivalent circuit model; identification; automotive drive cycle

1. Introduction

Over the past few decades, extensive research has been carried out to explore the applications of lithium ion batteries, which have been used in numerous applications [1,2]. As an example, combined with electric motors, Li ion batteries have been proven to be a reliable alternative for internal combustion engines (ICEs) as a source of electrical energy storage and delivery in vehicle propulsion systems. Considering the innate properties of the Li ion batteries such as high power and energy densities and extended cycle life, they are expected to play a critical role in the quest for alternate electric power sources. Numerous chemical compositions have been experimentally tested for Li ion cells to improve their performance measures such as specific power, specific energy, safety, cost, and life span [2,3].

Li ion cells are currently being extensively used in the development of automotive batteries due to their capacity to store higher energy and their ability to quickly charge and discharge [4]. As concluded in [5–7], the performance of the Li ion batteries is greatly dependent on the operating temperature of the cell. The study further demonstrates that

the output power and the capacity of the cells are significantly reduced when the operating temperature crosses 50 °C. At temperatures beyond the maximum permissible window, decomposition of the solid electrolyte interface is observed. This results in the absence of protection between the electrode and electrolyte, leading to the release of oxygen and other gases, which can cause thermal runaway [8]. An LFP cell undergoes phase change under various stages of lithiation [9], thus not emitting oxygen at higher temperatures. On the opposite end of the spectrum, when the operating temperature is below the minimum level of the allowable temperature, the deposition of metallic lithium is observed on the anode. The formation of such structures is called lithium plating [10], which causes a drop in the performance of the cell, finally leading to cell ageing. In another study [11], it was observed that a drop in the ambient temperature and an increase in the C rate led to a reduction in the available state of charge (SoC). These conditions put forward the need for analysing the thermal behaviour of the Li ion cells, as it helps in estimating the rise in the temperature when the cell is subjected to different operating conditions.

In addition to the electrochemical cell models, although very accurate, include complexities. Therefore, other modelling approaches such as equivalent circuit models (ECMs) are introduced, consisting of electrical circuit elements [12]. That approach is extensively implemented using resistors and capacitors to determine the voltage dynamics of both Li ion and voltage-regulated lead acid batteries [13,14]. A first-order equivalent electrical circuit model, employing a single RC model, was implemented in [8] in developing an electrical model of a 26650 LFP cell.

In the present study, ANSYS 2024 R1 Fluent is used as a finite element solver. The software expects the cell parameters as the inputs to be used in a second-order equivalent circuit model consisting of OCV, ohmic resistance, and two RC circuits. Those electrical parameters are found for the LFP cell based on experimental tests, and they are inserted into the ANSYS software. Then, a thermal analysis of the cell is carried out using the battery model available. In this study, a lumped electrochemical thermal model is used to carry out the analysis and determine the thermal characteristics of the LFP cell. Most of the thermal model's parameters are extracted from the literature and then inserted into the software. Finally, the proposed model is validated against the temperature data collected during the experimental tests.

The novelties of this study can be summarised as follows:

- A couple of new LFP cell electrothermal models are developed and simulated using ANSYS.
- A real automotive duty cycle is used for the validation of the proposed cell thermal model under a dynamic load profile.
- The solve design optimisation technique for ECM parameter identification is validated using experimental data, and its usability in cell temperature estimation is tested.

2. Cell Specifications and Experimental Tests

2.1. Lithium Iron Phosphate (LFP) Cell Specifications

The construction of the Li ion cells is classified into three categories, namely cylindrical, prismatic, and pouch cells [15]. The nomenclature of a cylindrical cell is performed in a way that represents the dimensions of the cell. For example, an 18650 cell represents a cell with an 18 mm outer diameter and a total height of 65 mm. The current study is focused on a 26650 cylindrical Li ion cell as obtained from RS Pro. The cell has an outer diameter of 26.2 ± 0.01 mm and a height of 65.6 ± 0.4 mm [16]. Lithium (L) iron (Fe) phosphate (P) (LFP) is the material of the cathode in the cell, with graphite being the anode. Table 1 highlights the key performance specifications of the cell. These values are critical to understanding the operating conditions of the cell. They also enable the battery manufacturers to compare the

capabilities of different Li ion cells based on their chemical compositions and extract their peak performances.

Table 1. LFP cell specifications [16].

Specification	Value
Voltage (nominal)	3.2 V
Capacity	3300 mAh
Maximum cut-off voltage	3.65 ± 0.05 V
Minimum cut-off voltage	2.5 V
Maximum continuous discharge current	9.6 A
Pulse discharge current	15 A, 10 s
Operating temperature	Charging: 0–55 °C Discharging: 20–60 °C
Weight of the cell	86 g

2.2. Cell Testing

The LFP cell was tested under the Worldwide Harmonised Light Vehicles Test Procedure (WLTP). The WLTP cycle was introduced in 2017 to replace the New European Driving Cycle (NEDC) [17]. It became mandatory to test all the internal combustion engine vehicles on that cycle in Europe since then. In the case of EVs, the cycle is used to determine the range of the vehicle. The key advantage of this cycle is its dynamic nature to simulate highly realistic driving conditions. In the experiments of this study, the corresponding WLTP current profile is obtained based on the simulation models presented in [18,19]. In [18,19], a full-vehicle powertrain model was simulated to determine the power demand from the battery. Using these data, the current and voltage requirements were calculated, which has been a common approach in the literature. The profile was scaled for a single LFP cell. The WLTP cycle is used as an example here because it is very well known by the automotive community. The key objective of this study was to estimate the temperature variations on the surface of the cell subjected to a duty cycle. Hence, other drive cycles or pulse tests could also be used to validate the models. In the current study, a fully charged cell is discharged by the WLTP current profile, continuing until the minimum cut-off voltage of the cell is reached.

Figure 1 indicates a schematic layout of the test setup and Figure 2 shows the battery test rig in detail, which consists of several components. The central component of the test rig is a PC, which is equipped with MATLAB/Simulink 2019a software and communication cables to communicate with the power supply and the thermo-couple data logger. The PC sends charge/discharge commands to the power supply, which then applies the required load current to the battery. The power supply is manufactured by Kepco company. The model which is used in this study is 50 A-20 V. The battery is located inside a thermal chamber to control the ambient temperature during the tests. To monitor the performance of the battery during the test, the power supply measures the battery voltage and current every second. This information is sent back to the PC for recording and monitoring purposes. In addition to measuring the battery voltage and current, the temperature signal is collected during the tests through two thermocouples of the same type attached on the surface of the cell. Two thermocouples were used to avoid any errors due to accuracy. The measured temperature from both thermocouples was the same. Hence, a single reading was extracted for data analysis.

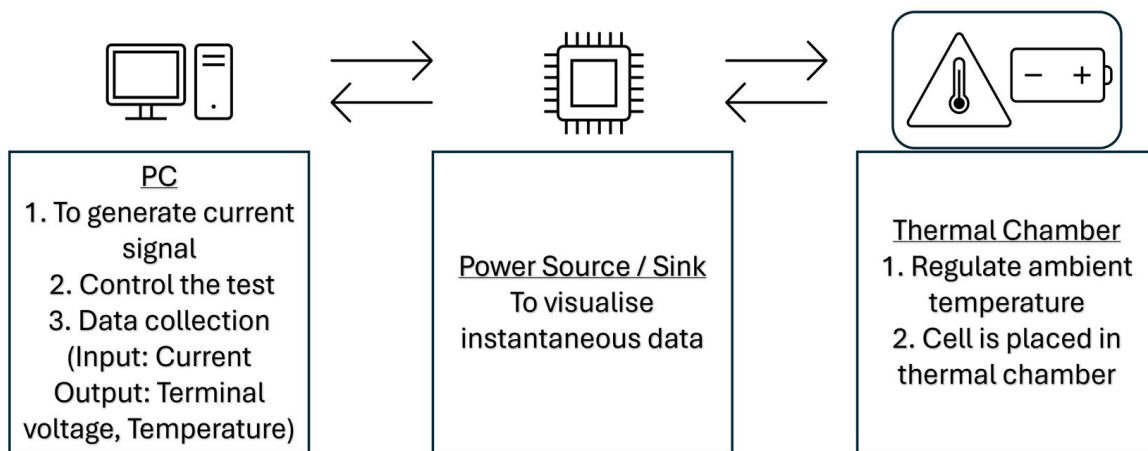


Figure 1. Schematic layout of the test setup.

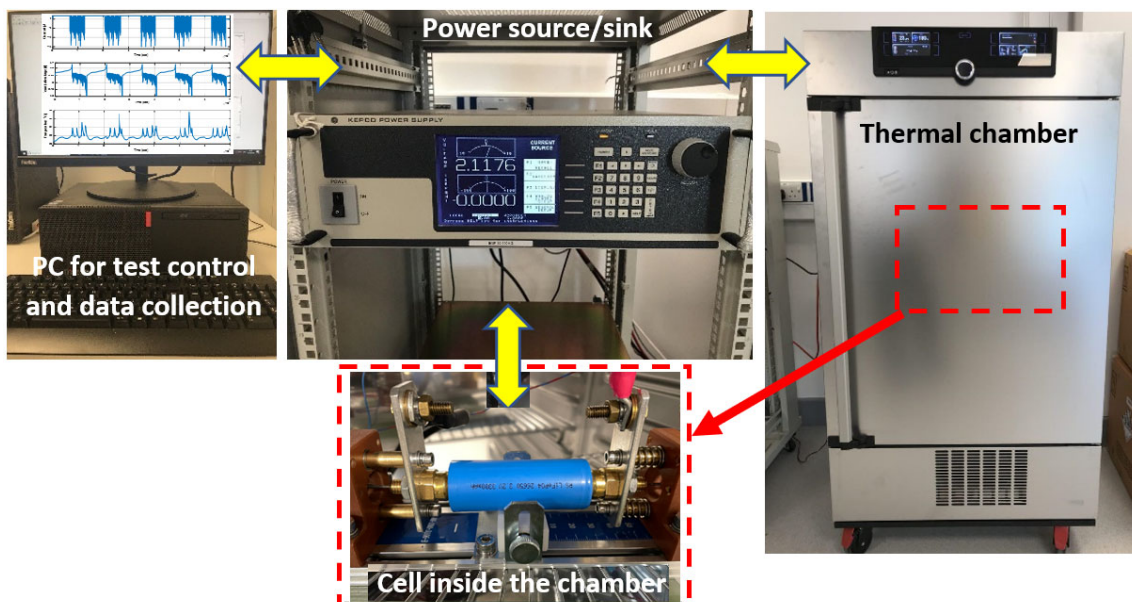


Figure 2. Experimental test setup used for LFP cell testing.

Figure 3 represents the WLTP load current profile applied to the LFP cell during an example discharge test, with negative current values representing the discharge mode, the cell's terminal voltage, and its surface temperature measurements. In that test, the WLTP discharge profile is started from 100% SoC, and it is repeated until the cell is fully depleted.

As seen in Figure 3, the peak discharge current of the WLTP test on the LFP cell is 15 A. According to the cell's specification sheet, the maximum continuous discharge current is 9.6 A, and the maximum pulse discharge current is 15 A for 10 s. However, in the WLTP profile, the peak discharge current of 15 A is applied only for a second, and the duty cycle is developed in such a way that continuous high discharge current is avoided. After each test, the cell goes to either the relaxation mode or is charged for the next cycle. The charging rate is 0.5 C (for 3.3 Ah, 1 C rate would indicate that the cell would charge/discharge completely in 1 h), and it continues until the cell's voltage reaches 3.65 V, showing it is fully charged.

In this experiment, the input is assumed to be the current signal, whereas the outputs are the cell's terminal voltage and its surface temperature, which are also shown in Figure 3. The terminal voltage is measured across the terminals of the cell, and the temperature signal is obtained via thermocouples placed on the cell casing's surface. All three signals are recorded at a rate of 1 Hz.

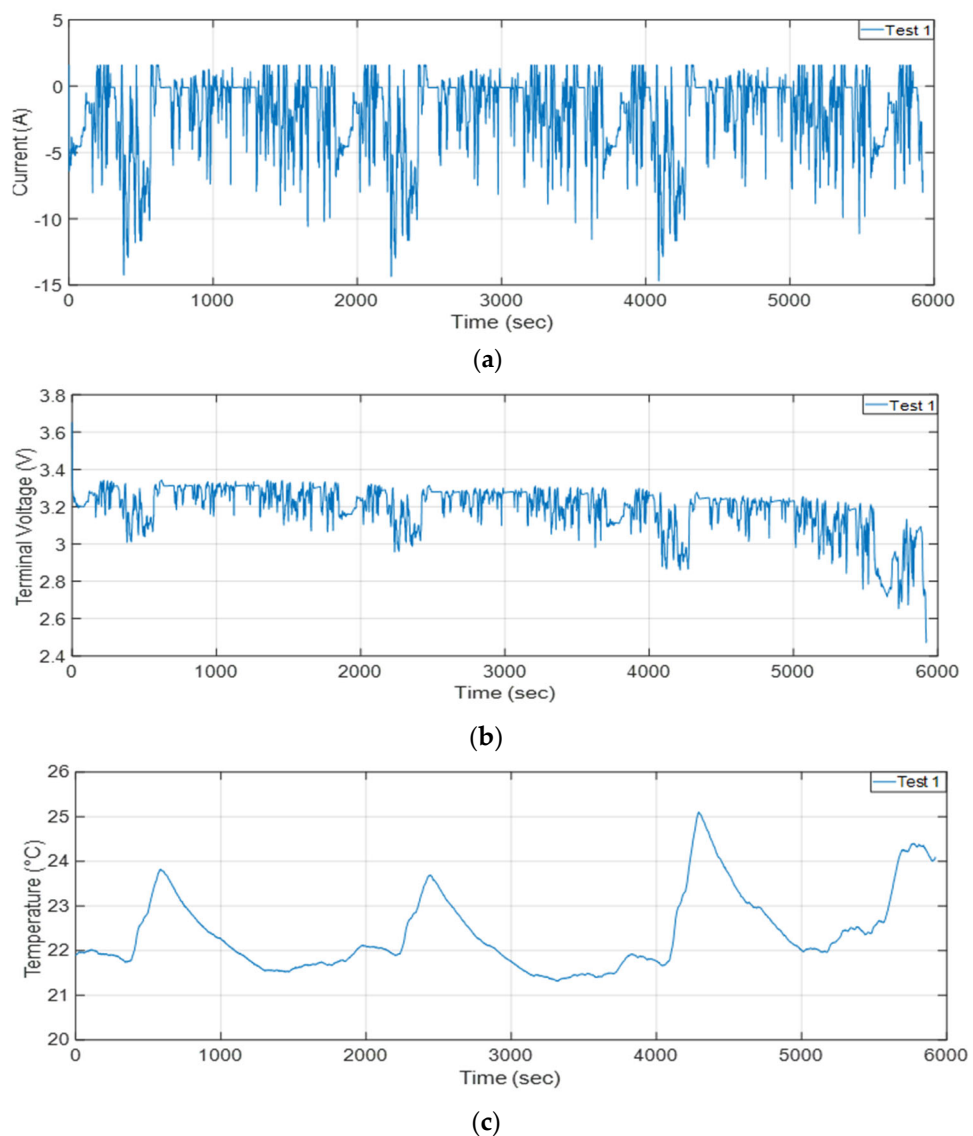


Figure 3. LFP cell's (a) current, (b) voltage, and (c) temperature measurements during a WLTP discharge test.

Looking at the terminal voltage data, they instantly change in response to the changes in the current signal, which is a common behaviour observed in batteries. During the discharge tests, the cell is operated between the maximum and the minimum cut-off voltages, which are 3.65 V and 2.5 V, respectively. As the cell is charged, the voltage steadily increases from 2.5 V to 3.65 V.

From Figure 3, it can also be observed that the surface temperature of the cell fluctuates significantly as the cell is being discharged based on the WLTP profile. The trend of the temperature change highly correlates with the current signal, though with a time lag.

3. Modelling of the LFP Cell

Computer-Aided Three-Dimension Interactive Application (CATIA) Version 5 was used for the 3D modelling of the LFP cell. The 3D model was later imported into ANSYS to perform thermal and electrical analysis. Regarding the ANSYS simulation platform, we decided to use it simply because it is a famous software for finite element analysis, and there are several studies in the literature in which the same software is used. The diameter and height of the cell are obtained 26.2 mm and 65.6 mm, respectively, from the cell specification sheet [16]. However, the dimensions of the positive and the negative tabs were not specified.

Hence, these components are modelled as simple hollow cylinders for the simplicity of the model. As the cell is considered a single homogenous body in ANSYS [20], the intricate details of modelling the spirally wound jelly roll of a cylindrical cell are not needed. Using the battery model in ANSYS, a cell-level study can also be seamlessly expanded to module and pack-level models. In a similar study in the literature [21], a thermal analysis was conducted on an 18650 cylindrical lithium–cobalt oxide cell by considering a simplified circular structure instead of the entire jelly roll structure, which led to a simplified model. Using a similar approach as in [21], also in the present study, two iterations of the LFP cell design are proposed, and their corresponding results are discussed. The cell’s active zone comprises the jelly roll inserted in the casing. It is labelled as the active zone, as it is the section of the cell where the electrochemical reactions occur during the cell’s operation conditions, leading to heat generation. In the ANSYS solver, a homogenous structure is considered for the active zone; therefore, it was modelled as a single solid component. Finally, the accuracy of each CAD model is determined by comparing the simulated temperature with the reference temperature obtained from the test data.

3.1. LFP Cell 3D Modelling—Iteration 1

In the first iteration, the components of the cell are modelled as simple solid cylinders stacked upon each other to understand the propagation of the heat within the cell. The active zone is designed with a diameter of 26.2 mm, and the tabs are then assembled on it. Clearances are considered at the top and bottom of the active zone for the positive and negative tabs. The height of the cell from the extreme ends of the terminals is 65.6 mm. Considering 5 mm and 2 mm as the heights of the positive and negative tabs, respectively, the active zone is modelled with a height of 58.6 mm. According to the literature, the tabs could be modelled as either a solid or a hollow cylinder. Therefore, in the first iteration, solid cylindrical sections are defined to design the tabs. Figure 4 shows the cross-section and front view of the cell wall in Iteration 1. In addition, the top, front, and cross-section views of the positive and negative tabs in Iteration 1 are illustrated in Figures 5 and 6, respectively.

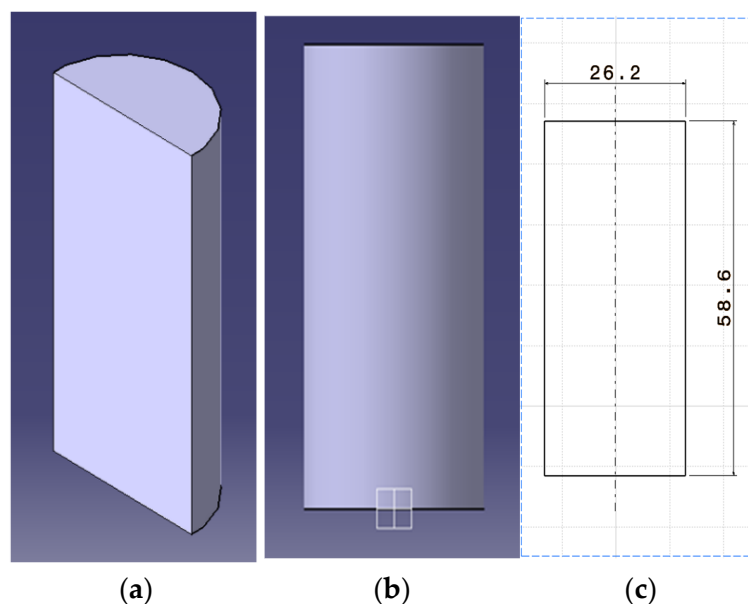


Figure 4. (a) Cross-section, (b) 3D front view, and (c) 2D front view of the cell wall in Iteration 1.

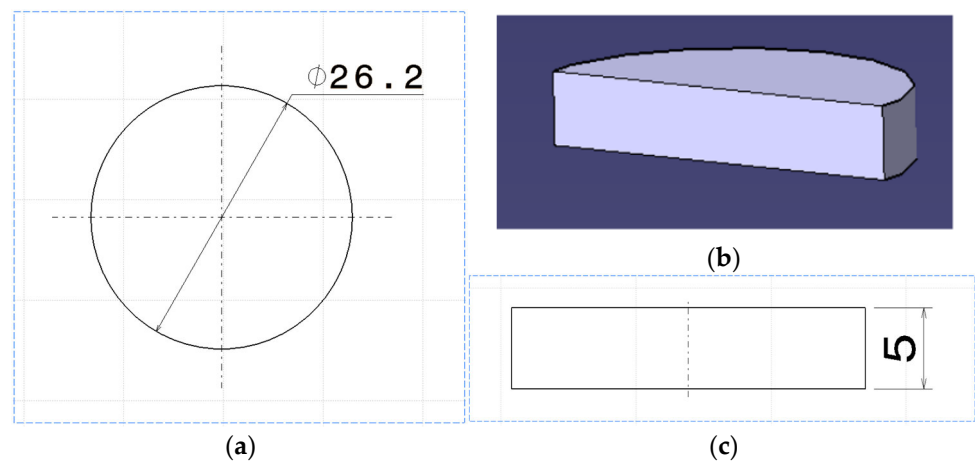


Figure 5. (a) Top, (b) cross-section, and (c) front views of the positive tab in Iteration 1.

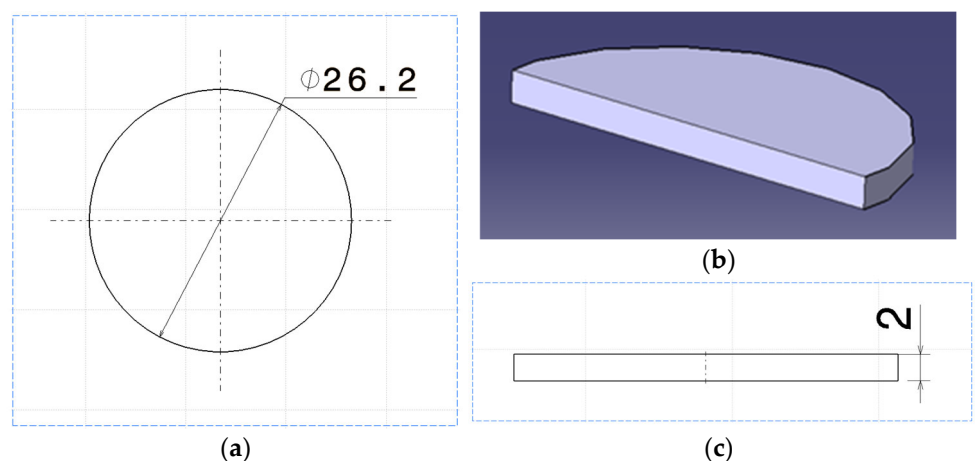


Figure 6. (a) Top, (b) cross-section, and (c) front views of the negative tab in Iteration 1.

3.2. LFP Cell 3D Modelling—Iteration 2

The second iteration involves building a more realistic model of the cell by taking the available dimensions into consideration, inspired by the cross-section of the actual cell. Against Iteration 1, in which solid cylindrical sections are defined, hollow cylindrical clearance with a common diameter of 20 mm is considered for the tabs in this iteration. Assuming a total height and clearance of 1 mm and 0.5 mm for the positive and the negative tabs, respectively, the active zone has been designed with a height of 64.1 mm. The outer diameter of the cell is set to 26.2 mm, according to the cell's specification sheet. The hollow cylindrical structure is used for both tabs. An external diameter of 19.7 mm is considered with a clearance of 0.3 mm to avoid interfacing issues in ANSYS. The tabs are modelled with a wall thickness of 0.85 mm. The thicknesses of the positive and negative tabs are 0.85 mm and 0.5 mm, respectively. Finally, the height of the positive and negative tabs are 0.5 mm and 1 mm, respectively. Clearances have been considered to address the safety components such as a positive thermal coefficient (PTC), a gasket, and a gas release vent. However, another study [21] suggested that these components do not significantly impact the thermal investigation of the cell, considering the size of the cell.

Figure 7 shows the cross-section and front view of the cell wall in Iteration 2. In addition, the top, front, and cross-section views of the positive and negative tabs in Iteration 2 are illustrated in Figures 8 and 9, respectively.

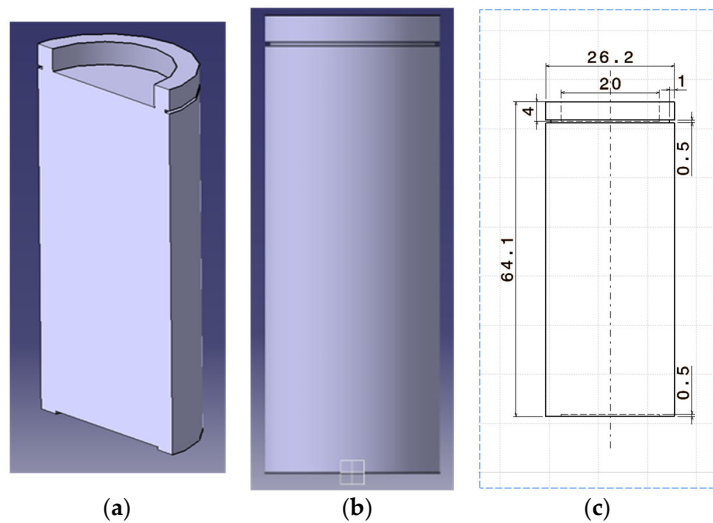


Figure 7. (a) Cross-section, (b) 3D front view, and (c) 2D front view of the cell wall in Iteration 2.

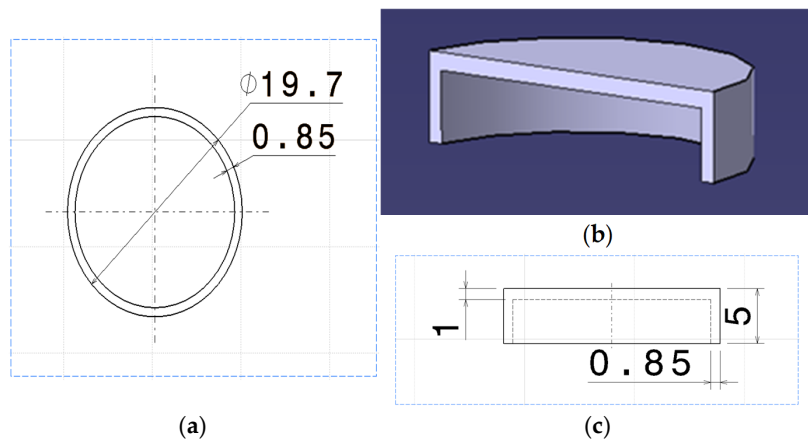


Figure 8. (a) Top, (b) cross-section, and (c) front views of the positive tab in Iteration 2.

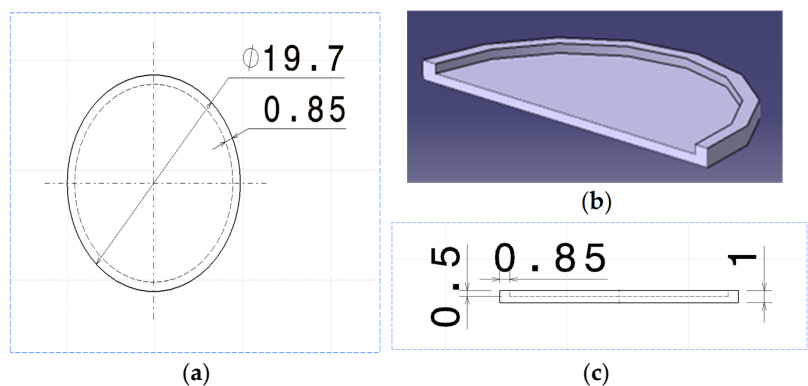


Figure 9. (a) Top, (b) cross-section, and (c) front views of the negative tab in Iteration 2.

3.3. Cell Assembly

For each of the two iterations mentioned above, the active zone, the positive tab, and the negative tab are assembled. The tabs are assembled to the active zone using assembly constraints. The constraints are defined to align the individual components with each other with respect to axis, distance, and inclination. Coincidence constraint is used to ensure that all three components are on the same plane. An offset constraint is used to define the distance between each of the two surfaces. In a cell, the surface of the tabs and the active

zone are in contact with each other. Thus, an offset of 0 mm is considered. Figures 10 and 11 indicate the external dimensions and cross-section structure of the cell for Iteration 1 and Iteration 2, respectively.

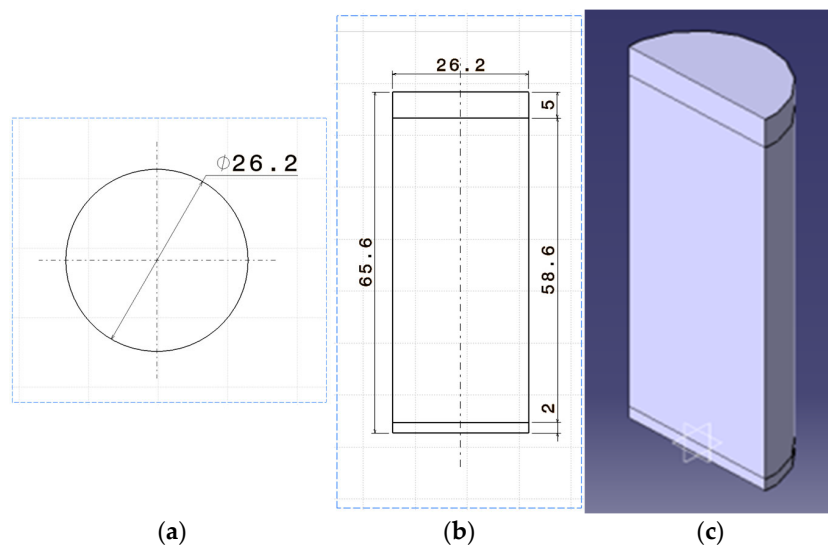


Figure 10. (a) Top, (b) front, and (c) cross-section views of cell assembly in Iteration 1.

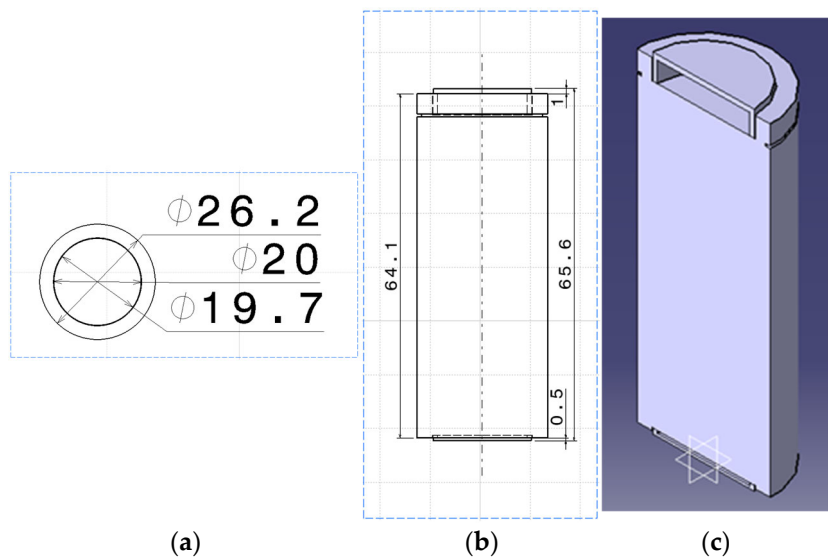


Figure 11. (a) Top, (b) front, and (c) cross-section views of cell assembly in Iteration 2.

4. Finite Element Analysis (FEA) of the LFP Cell Model

4.1. ANSYS Fluent

The ANSYS Fluent software package consists of four solution methods to simulate the thermal behaviour of a system. Furthermore, the software has four sub-models to evaluate the electrochemical behaviour of the cell [20]. The methods of thermal behaviour analysis are (1) the conjugate heat transport (CHT) coupling method, (2) the functional mock-up unit (FMU)–CHT coupling method, (3) the circuit network solution method, and (4) the multi-scale multi-domain (MSMD) solution method. Methods 1 and 2 are not suitable for this application, since the electrochemical characteristics of the LFP cell are not determined using ANSYS Fluent. On the other hand, in the circuit network solution method, the heat generation is assumed to be constant throughout the cell; however, this assumption cannot be valid in battery cells, as the generated heat may not be uniform. Regarding the last option,

the key advantage of the MSMD method is that it can deal with multiple domains, which are the particle domain, electrode domain, and cell domain, making it suitable for multi-physics study [22]. As a result of this, the MSMD method can solve the temperature distribution equations within a cell. Therefore, the MSMD method is selected in this study, with the only downside being a higher computational cost, as additional equations need to be solved.

To simulate the electric behaviour of the cell, ANSYS offers four sub-models [20], namely (1) the Newman, Tiedeman, Gu, and Kim (NTGK) model; (2) the equivalent circuit model (ECM), (3) the Newman pseudo-2D (P2D) model, and (4) the user-defined model. Amongst the available options, the ECM sounds to be ideal for our simulation condition with frequent changes in the current signal. In fact, the NTKG model is only efficient under uniform electric load conditions. On the other hand, the P2D model is accurate, as it solves numerous equations; however, it needs more computational resources, which are not necessarily available in this application. Regarding the fourth option, a user-defined model just adds more complexity to the model. Therefore, an ECM would be the ideal solution by considering its versatility not only for being able to deal with both individual cells and battery packs but also its ability to solve numerous cell chemistries. By default, ANSYS uses a second-order ECM consisting of two RC circuits using a study [23].

In summary, the MSMD solution method, coupled with the ECM, is implemented in this study. In the following sections, further details of the FEA model of the LFP cell in ANSYS are explained.

4.2. Meshing

ANSYS workbench meshing is used to discretise the design iterations into smaller elements. Generally, in FEA, the size and the type of the applied mesh can significantly influence the accuracy of the solution. As the total length of the cell is 65.6 mm, the meshing process is iterated by starting off with a coarser minimum mesh size of 1 mm to a finer mesh size of 0.5 mm. The mesh error metrics are then used to find the optimal mesh size. The magnitude of the metrics directly influences the accuracy of the model solved in the fluent solver. The ANSYS workbench meshing technique is chosen over the fluent meshing technique since the latter results in generating disconnected continuous surfaces, which the MSMD model cannot resolve. Tetrahedral and hexahedral elements are generated using the workbench meshing method. The modelled cell assembly is redefined into groups using the named selections, including (1) the active zone, (2) positive tab, (3) positive tab wall, (4) negative tab, and (5) negative tab wall. The defined selections are then used to apply boundary conditions specific to each zone during the analysis setup. Among the available mesh error metrics, the minimum orthogonality, the maximum skewness, and the maximum aspect ratio are considered to ensure that the generated mesh is structured, which is critical for an accurate FEA. Table 2 [24] lists the acceptable ranges of the error metrics for the meshing. The element size in the design iterations is iterated to obtain the optimal values.

Table 2. Mesh metrics and their range.

Mesh Metric	Optimal Value	Acceptable Value	Poor Elements
Orthogonality	1	1–0.15	<0.15
Skewness	0	0–0.85	>0.85
Aspect Ratio	1	1–1000	>1000

4.2.1. LFP Cell Meshing—Iteration 1

In the first iteration, cell meshing is carried out upon defining the grouped selections mentioned previously. Additionally, face meshing is also defined on the surfaces of the

positive and negative tabs to ensure that the mesh is fine at the operating regions. The mesh size varies from 1 mm to 0.5 mm, and each case is analysed. It was observed that all the mesh size iterations satisfy the metrics. However, upon conducting the analysis, it was observed that for the coarser mesh sizes, i.e., 1 mm and 0.9 mm, the mesh metrics in Table 2 were not satisfied, as the solver failed to solve the heat generation equations that resulted in inaccurate temperatures. Starting from 0.8 mm and reducing further, the estimated temperatures are close to the reference values, which are obtained from the test data. The mesh size of 0.7 mm is found to be the optimal size by considering the accuracy of the results and the computational efficiency. Figure 12 illustrates the LFP cell model meshing in Iteration 1.

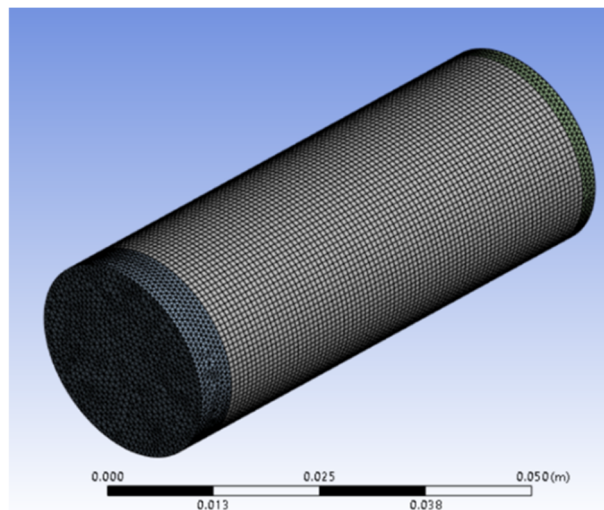


Figure 12. LFP cell model meshing—Iteration 1.

4.2.2. LFP Cell Model Meshing—Iteration 2

A similar strategy is adopted for the second iteration of the LFP cell model meshing, as explained in the previous section. The big difference here is that the second cell model is used as described in Section 3. Again, the mesh metrics are observed to be complying with the measures presented in Table 2. Figure 13 illustrates the LFP cell model meshing in Iteration 2.

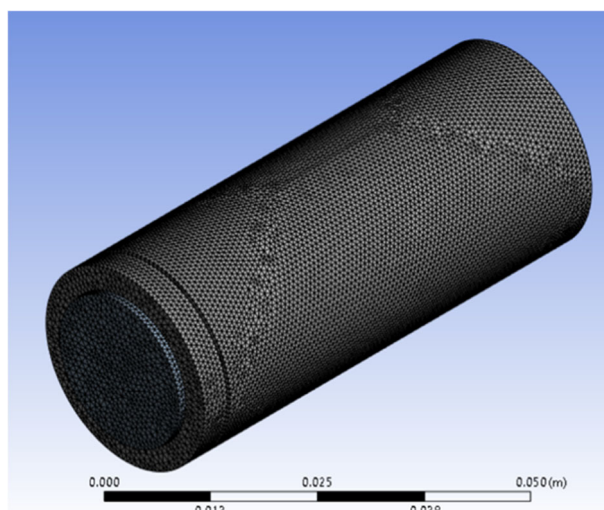


Figure 13. LFP cell model meshing—Iteration 2.

4.3. Background of the Solution Method

Both the cell modelling iterations are set up with the same conditions in the battery model. To simulate the thermal and electrical behaviours of the cell, an electrochemical model coupled with a lumped thermal model is used by the solver. As stated earlier in Section 4.1, four solution methods are provided by ANSYS Fluent to resolve this simulation case study. The MSMD solution method was selected in this study because of the reasons discussed in Section 4.1. The thermal and electrical differential equations used in the MSMD method are provided in the ANSYS software's guide as follows [20]:

$$C_p \times \frac{\partial \rho T}{\partial t} - \nabla \times (k \nabla T) = \sigma_+ |\nabla \varphi_+|^2 + \sigma_- |\nabla \varphi_-|^2 + \dot{q}_{Ech} + \dot{q}_{short} + \dot{q}_{abuse} \quad (1)$$

$$\nabla \times (\sigma_+ \nabla \varphi_+) = -(\dot{j}_{Ech} - \dot{j}_{short}) \quad (2)$$

$$\nabla \times (\sigma_- \nabla \varphi_-) = \dot{j}_{Ech} - \dot{j}_{short} \quad (3)$$

$$\dot{j}_{Ech} = I \times \left(\frac{Q_{Nominal}}{Q_{ref} \times Vol} \right) \quad (4)$$

$$\dot{q}_{Ech} = \dot{j}_{Ech} \times \left[V_{ocv} - V - \left(T \times \frac{dU}{dT} \right) \right] \quad (5)$$

The parameter \dot{q}_{abuse} is set to zero for normal operating conditions. In the absence of an internal short-circuit, j_{short} and \dot{q}_{short} , are equivalent to zero. Equations (4) and (5) are used by the solver to determine j_{Ech} and \dot{q}_{Ech} . In both modelling iterations, the same theoretical equations are used. The cell used in these experiments was a relatively newer cell with a shorter cycle life, and the same model parameters were used for model development. Hence, upon testing, the capacity of the cell was the same as highlighted by the cell manufacturer, $Q_{Nominal} = Q_{ref} = 3.3$ Ah.

4.4. Electrical Parameters

The electrical circuit model is a very common model for batteries in the literature. The other reason we selected that model was its availability in the ANSYS software. Here, the LFP cell is tested, and then the model is parameterised in ANSYS. The default ECM used in ANSYS Fluent is a second-order model with two RC networks, as shown in Figure 14. The model's parameters include the open circuit voltage (V_{ocv}), the ohmic resistance (R_s), and the two RC parallel circuits' parameters R_1 , R_2 , C_1 , and C_2 [25]. The parameter R_1 is the charge transfer resistance, and the parameter C_1 is the electrochemical double-layer capacitance. Together, R_1 and C_1 describe the rapid dynamics of the battery, depicting the surface effects on the electrodes and reaction kinetics. On the other hand, R_2 and C_2 encapsulate the effect of the diffusion processes on the electrolyte and the active material [23]. The time constants of the two RC networks are determined by the product of the resistance value with its corresponding capacitance value. It is used to signify the internal dynamics of the cell during rapid dynamics and slow diffusion processes [23,26].

According to the literature [27], the second-order ECM is an ideal electrical battery model when considering a trade-off between accuracy and computational resources. The cell's state of charge is determined using the Coulomb counting method. The cell parameters are estimated as a function of SoC using the following equations [20]:

$$V = V_{ocv}(SoC) - V_1 - V_2 - (R_s(SoC) \times I(t)) \quad (6)$$

$$\frac{dV_1}{dt} = -\frac{1}{R_1(SoC)C_1(SoC)}V_1 - \frac{1}{C_1(SoC)}I(t) \quad (7)$$

$$\frac{dV_2}{dt} = -\frac{1}{R_2(\text{SoC})C_2(\text{SoC})}V_2 - \frac{1}{C_2(\text{SoC})}I(t) \quad (8)$$

$$\frac{d(\text{SoC})}{dt} = \frac{I(t)}{3600 \times Q_{\text{ref}}} \quad (9)$$

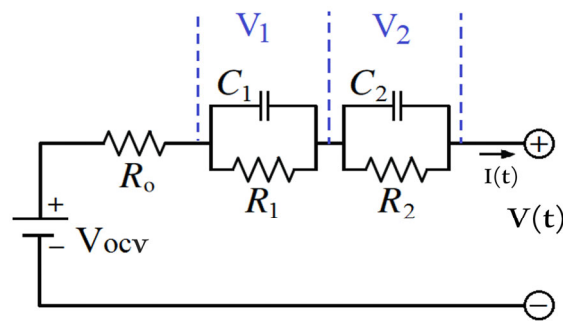


Figure 14. The 2nd-order ECM used in ANSYS.

4.5. System Identification

As explained in Section 4.4, ANSYS expects the user to provide second-order ECM data to resolve the electrical and thermal characteristics of the cell. Using the procedure discussed in [27], a discharge pulse test is conducted in the current study to obtain the ECM parameters of the cell from test data. The pulse test was also conducted at 20 °C, the same temperature as the WLTP test. The solve design optimisation (SDO) technique is utilised in the current study. The SDO technique is adapted by Mathworks in estimating the ECM data for a cell utilising the PulseSequence object defined in MATLAB libraries [28]. The advantage of this technique is that it can be expanded from one RC to up to five RC networks. However, considering the model required in ANSYS and based on the literature, a two-RC model is chosen here as a proper trade-off between accuracy and complexity. In this optimisation technique, the pulse discharge profile is split into individual pulses by considering the current threshold, as shown in Figure 15, where a positive value means discharge load current being applied to the cell and a zero value indicates relaxation mode.

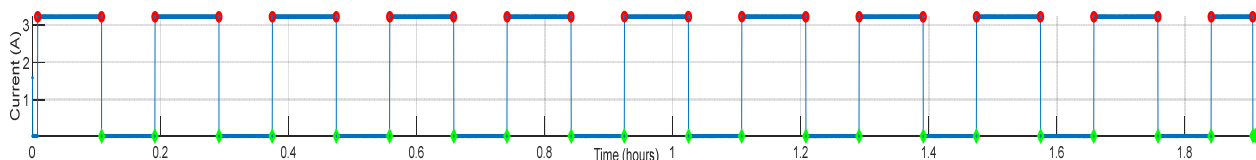


Figure 15. Pulse segmentation based on the current signal.

The ECM parameters are then calculated by applying a series of numerical optimisation iterations utilised by the SDO technique. After running the optimisation code, the mean residual voltage between the test data and the simulated data was obtained as 4.54 mV, demonstrating a good level of accuracy. The LFP cell parameter values of V_{OCV} , R_s , R_1 , R_2 , C_1 , and C_2 are illustrated in Figure 16 with respect to the cell's SoC.

Using the ECM parameters obtained, the cell's terminal voltage was obtained using the two-RC model in Simulink [29]. The mean difference in terminal voltage upon comparing the simulated data with the test data is 3 mV. Figure 17 compares the simulated data against the experimental measurement during an example pulse discharge test.

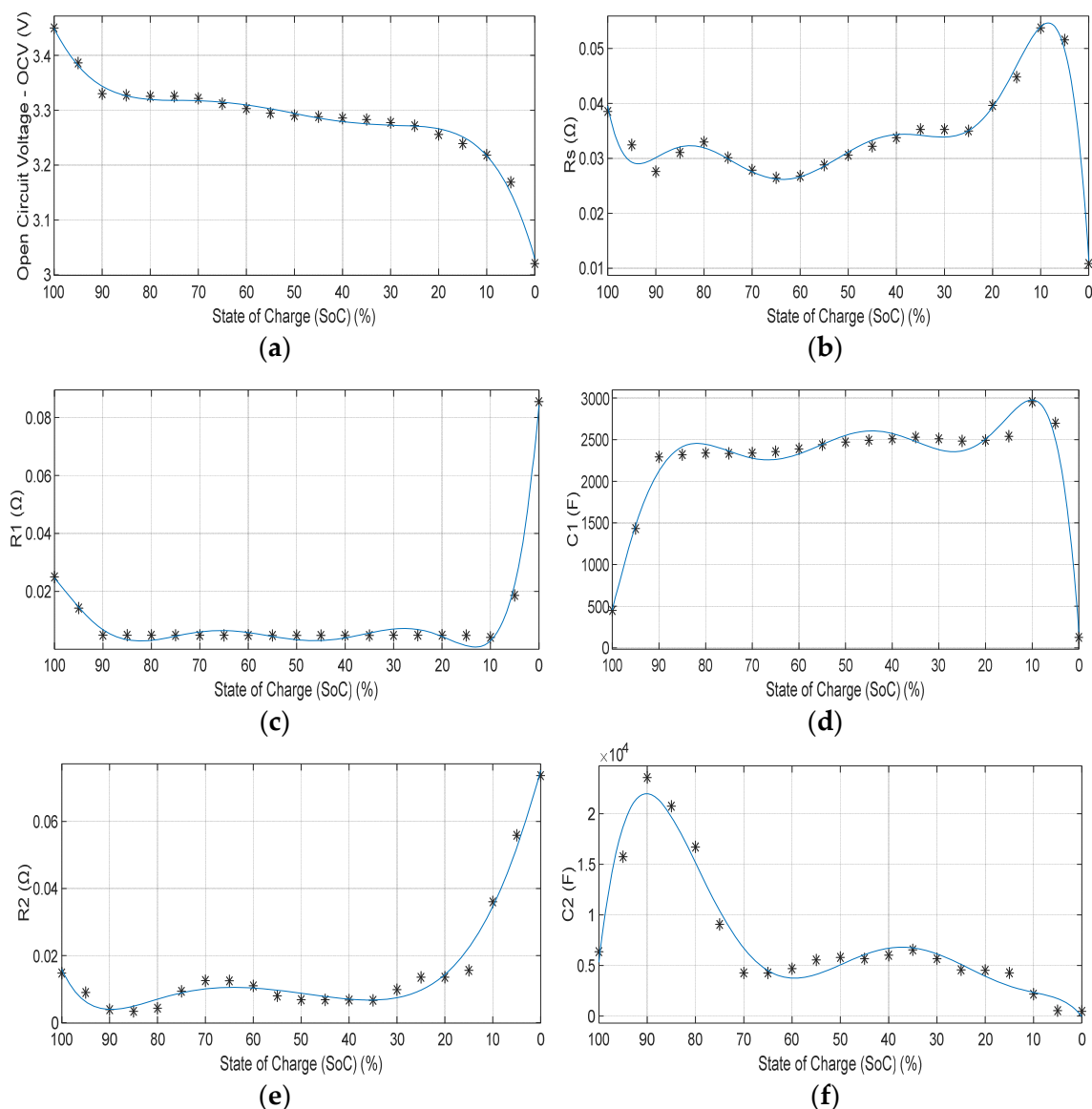


Figure 16. LFP cell's ECM parameters vs. SoC including the data points and the fitted polynomials: (a) open circuit voltage, (b) ohmic resistance, (c,d) 1st RC network parameters, and (e,f) 2nd RC network parameters.

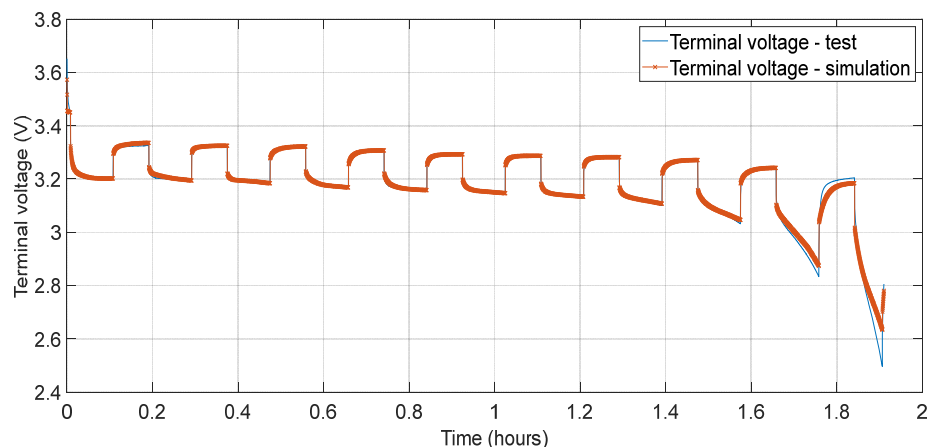


Figure 17. Validating the simulated terminal voltage against experimental data.

4.6. Material Properties

As discussed earlier, the active zone of the model encompasses the electrodes and the separator. However, because the entire battery is considered a homogenous unit in ANSYS, the individual components are not resolved. In fact, all the layers of the cell are not necessary to perform the simulation [20]. Therefore, the lumped approach is utilised to define the properties of the active material. These values can vary from manufacturer to manufacturer, despite having the same composition and overall specifications. In the present study, the LFP cell's material properties are extracted from the experiments conducted in [30], in which a 2.6 Ah 26650 LFP cell has been tested. The thermal parameters of the cell's active zone are presented in Table 3.

Table 3. Thermal parameters of the active zone [30].

Parameter	Representation	Value
Density	ρ	$2047 \text{ kg} \times \text{m}^{-3}$
Specific heat coefficient	C_p	$1109.2 \text{ J} \times \text{kg}^{-1} \times \text{K}^{-1}$
Thermal conductivity	k	$0.610 \text{ W} \times \text{m}^{-1} \times \text{K}^{-1}$
Heat transfer coefficient	h	$58.6 \text{ W} \times \text{m}^{-2} \times \text{K}^{-1}$

The user-defined scalar (UDS) values of electrical conductivity defined for the positive and negative potential, namely UDS-0 and UDS-1, are extracted from ANSYS tutorials with the values of $1.19 \times 10^6 \text{ S/m}$ and $9.83 \times 10^5 \text{ S/m}$ [20], respectively. Upon specifying the positive and negative tabs as the passive components, the material properties are then defined. The positive tab is generally made of aluminium, whereas the negative tab is made of copper [31]. Their respective thermal properties are defined using the material database available in ANSYS Fluent. Similarly to the active zone, the value of the electrical conductivity is taken from the ANSYS tutorial. However, a constant value of $1 \times 10^7 \text{ S/m}$ is defined for both tabs. The thermal properties of the positive and the negative tabs are presented in Tables 4 and 5, respectively.

Table 4. Thermal properties of the positive tab.

Parameter	Symbol	Value
Density	ρ	$2719 \text{ kg} \times \text{m}^{-3}$
Specific heat coefficient	C_p	$871 \text{ J} \times \text{kg}^{-1} \times \text{K}^{-1}$
Thermal conductivity	k	$202.4 \text{ W} \times \text{m}^{-1} \times \text{K}^{-1}$

Table 5. Thermal properties of the negative tab.

Parameter	Symbol	Value
Density	ρ	$8978 \text{ kg} \times \text{m}^{-3}$
Specific heat coefficient	C_p	$381 \text{ J} \times \text{kg}^{-1} \times \text{K}^{-1}$
Thermal conductivity	k	$387.6 \text{ W} \times \text{m}^{-1} \times \text{K}^{-1}$

4.7. Boundary Conditions

Defining the boundary conditions to the model is critical in any FEA. These conditions are implemented to specify the interaction between the model and its environment. Upon defining correct boundary conditions, the equations of the model are resolved to produce results that depict the realistic behaviour of the system. To analyse the heat generation through the surface of the cell, the conductive thermal properties of the surfaces are defined at the walls of the cell as well as the positive and the negative tabs. Under the convection thermal condition, the heat transfer coefficient and free stream temperature are defined.

The values presented in Table 6 are implemented at the walls of the cell as well as the tabs. Despite having the same composition, the value of the heat transfer coefficient (h) varies based on the cell manufacturer and the overall capacity. The value of 58.6 for the heat transfer coefficient is extracted from the experiments conducted in [30]. To validate the value of the heat transfer coefficient used in this paper, a sensitivity analysis was conducted by iterating the value by $+/-20\%$. Upon comparing the models' outputs and the experimental data, 58.6 resulted in minimal errors.

Table 6. Boundary conditions.

Parameters	Value
Heat transfer coefficient (h)	$58.6 \text{ W} \times \text{m}^{-2} \times \text{K}^{-1}$
Free stream temperature	20°C

Finally, the setup of the FEA model is concluded by eliminating the convergence criteria to ensure that the automatic convergence is avoided by the solver. Approximately 18 iterations per timestep is found to be optimal by considering the accuracy of the heat captured and the computational time taken.

5. Results and Discussion

As mentioned earlier, battery thermal management is quite critical in almost all applications of batteries. Heat generation in the cells should be analysed to predict the temperature changes in the cell under different operating conditions. In this study, a thermal analysis of a 26650 LFP cell was carried out, subjected to the WLTP discharge test. As explained in previous sections, two iterations of cell modelling are performed based on solid and hollow tab design concepts. The battery model available in ANSYS Fluent was used to simulate the thermal behaviour of the cell under the test conditions. The cell temperature is usually not equivalently distributed over the cell's surface; therefore, the area-weighted average method was used. This section is aimed at summarising the simulation results obtained from the models built in ANSYS. MATLAB software is also used for post-processing of the results where the simulated data are compared against the collected test data. The average error and the maximum error criteria are calculated to quantify the accuracy of the models. The cell's surface temperature is estimated using Equation (1). The abusive and short-circuit heat generation rates are ignored because the operating temperature of the tests was well within the ideal operating range. Therefore, the heat generation rate is assumed to be a function of electrical conductivity, phase potential, and heat generated due to electrochemical reactions.

5.1. Cell Temperature Estimation—Iteration 1

The analysis is initiated from the first discharge test having an initial SoC of 100%. Five tests are conducted for each iteration model for the sake of validation. Figure 18 illustrates the LFP cell's surface temperature obtained during the first discharge test from the first model built in ANSYS and the test data. As seen in Figure 18, during the discharge phase, the temperature fluctuates a lot because the current is withdrawn from the cell based on the WLTP drive cycle. Simulation results are compared against the experimental data to evaluate the accuracy of the model in Iteration 1. According to Figure 18, it is concluded that the simulated and the experimental temperature signals have a very similar trend, though there are some differences as well. The mean value of the error at each time step is obtained using MATLAB to determine the accuracy of the model. During Test 1, an absolute mean error of 0.08°C is obtained for the model in Iteration 1. Furthermore, the maximum

error is obtained to be $1.09\text{ }^{\circ}\text{C}$. The mean error, maximum error, and peak temperature during all five discharge tests are listed in Table 7.

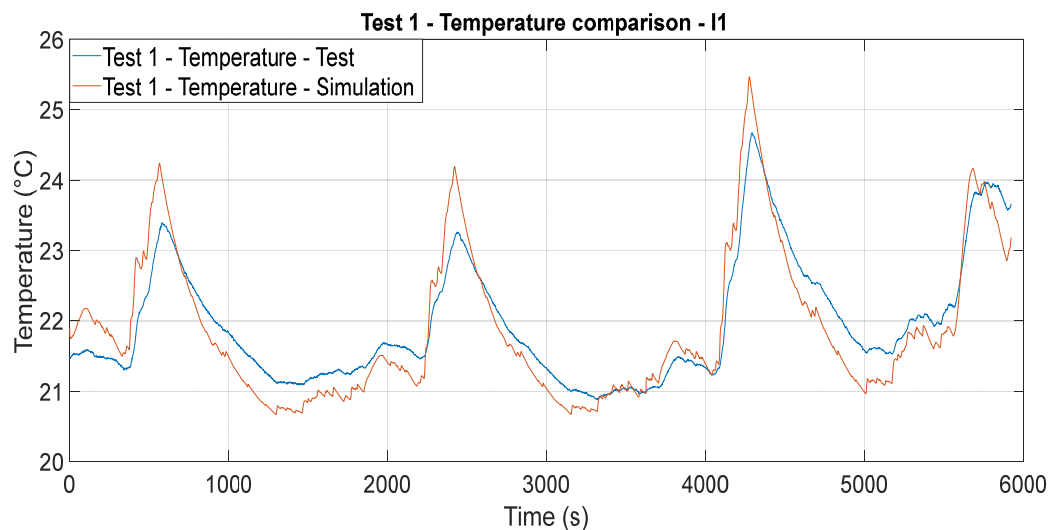


Figure 18. LFP cell temperature estimation validation against experimental data in Iteration 1.

Table 7. Error measurements for the cell model in Iteration 1.

Discharge Test	Absolute Mean Error ($^{\circ}\text{C}$)	Maximum Error ($^{\circ}\text{C}$)	Peak Temperature ($^{\circ}\text{C}$)
1	0.08	1.09	25.46
2	0.22	1.26	27.03
3	0.06	2.51	25.58
4	0.26	1.34	26.42
5	0.04	3.14	26.27

5.2. Cell Temperature Estimation—Iteration 2

A similar temperature simulation is performed in this section; however, the model developed in Iteration 2 is used. The cell model in Iteration 2 was designed based on the available dimensions and the cross-section of the cell as discussed in Section 3. The cell tabs are modelled as simple hollow cylinders, as suggested in [21]. Figure 19 illustrates the LFP cell's surface temperature obtained from the second model built in ANSYS and the test data. Again, several fluctuations are observed because of the WLTP discharge profile. A peak temperature of $26.79\text{ }^{\circ}\text{C}$ is observed amongst all five tests, and the final relaxation temperature is recorded at $21.4\text{ }^{\circ}\text{C}$. Simulation results are compared against the experimental data to evaluate the accuracy of the model in Iteration 2. According to Figure 19, there is again a good match between the simulated and experimental temperature values with an absolute mean error value of $0.36\text{ }^{\circ}\text{C}$. Comparing the results from Iterations 1 and 2, although the mean error has increased by $0.28\text{ }^{\circ}\text{C}$ in the second iteration, considering a more realistic cell model proved to be the iteration with potential for further research. The error values and the peak temperature of the cell during all discharge tests in Iteration 2 are mentioned in Table 8.

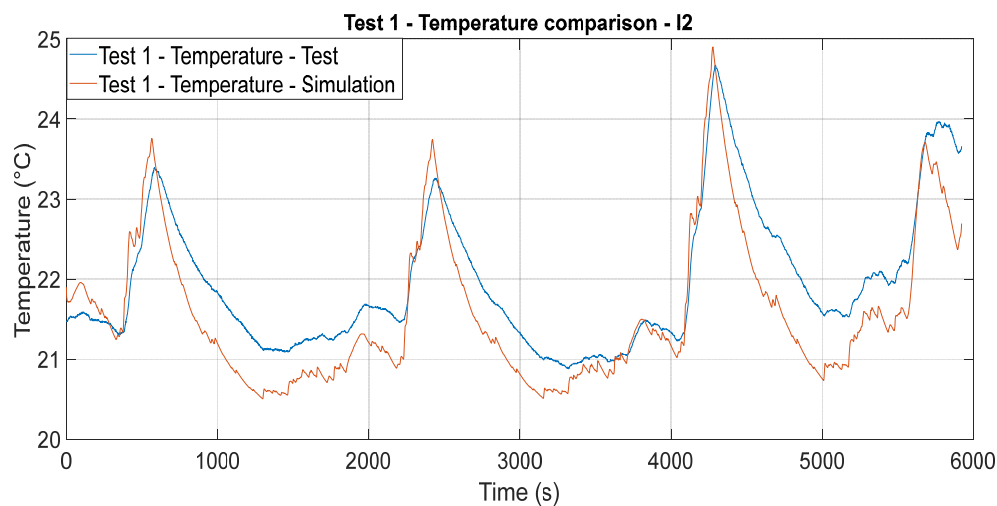


Figure 19. LFP cell temperature estimation validation against experimental data in Iteration 2.

Table 8. Error measurements for the cell model in Iteration 2.

Discharge Test	Absolute Mean Error (°C)	Maximum Error (°C)	Peak Temperature (°C)
1	0.36	1.24	24.90
2	0.48	1.50	26.33
3	0.33	1.96	25.02
4	0.51	2.00	25.77
5	0.32	2.54	25.67

6. Conclusions

A 26650 LFP cell was modelled and simulated in ANSYS Fluent for thermal analysis and temperature estimation. Two iterations of the cell model were developed and simulated according to an automotive drive cycle. Against Iteration 1, in which solid cylindrical sections were defined, in the second iteration, a hollow cylindrical clearance was considered for the tabs that made it more realistic. After trying several configurations, a mesh size of 0.7 mm was found to be the optimal size to generate tetrahedral and hexahedral elements to provide a discretised structure to the solver. The thermal and electrochemical parameters of the models were obtained from the literature as well as experimental test data. It was observed that the material properties and the heat convective coefficient affect the cell's heat generation significantly. Using the values obtained from the literature, both models resulted in a similar trend in temperature with respect to the test data. Average absolute error values of 0.13 °C and 0.40 °C were obtained for temperature estimation using the first and second iteration models, respectively. The mean error of less than 0.5 °C indicates a good match between the simulation and the test data. Such temperature estimation models could be used in the development of battery management systems (BMSs), ensuring that the battery cells are operating in safe conditions. Although the results were for an LFP cell, it is expected that the same methodology will be applied to other cell types as well.

Regarding the limitations of this study, one of the key challenges was to obtain the geometrical and effective cell parameters. A tear-down analysis could result in a more accurate model. However, considering the resources available, the parameters needed were used from the literature.

Author Contributions: Methodology, S.S.A. and A.F.; software, S.S.A.; validation, S.S.A. and H.Z.; formal analysis, S.S.A.; investigation, S.S.A. and A.F.; resources, A.F. and D.J.A.; data curation, H.Z. and S.S.A.; writing—original draft, S.S.A.; writing—review and editing, A.F. and D.J.A.; visualisation, S.S.A.; supervision, A.F.; funding acquisition, A.F. and D.J.A. All authors have read and agreed to the published version of the manuscript.

Funding: This work was co-funded by the UKRI Faraday Battery Challenge project (10048333) called Next Generation LFP Cathode Material (NEXLFP) and the UKRI-APC project (10078104) called High-performance LFP Cathode Active Material (HiCAM). In addition, Abbas Fotouhi acknowledges funding from the Faraday Institution (Industrial Fellowships FIIF-003 and FIIF-014).

Data Availability Statement: The data presented in this study will be available upon request from the corresponding author and from CORD at <https://doi.org/10.17862/cranfield.rd.24953571> after an embargo period (i.e., 1 February 2029).

Conflicts of Interest: The authors declare that the research was conducted in the absence of any commercial or financial relationships that could be construed as a potential conflict of interest.

Nomenclature

Symbols	Description
A	Ampere
Ah	Ampere-hour
°C	Degree Celsius
C ₁	Polarisation capacitance (F)
C ₂	Diffusion capacitance (F)
h	Heat transfer coefficient ($\text{W} \times \text{m}^{-2} \times \text{K}^{-1}$)
I	Current (A)
j _{Ech}	Volumetric current transfer rate due to electrochemical reactions ($\text{A} \times \text{m}^{-3}$)
j _{short}	Current transfer rate due to battery internal short-circuit ($\text{A} \times \text{m}^{-3}$)
q̇ _{Ech}	Electrochemical reaction heat($\text{W} \times \text{m}^{-3}$)
q̇ _{short}	Heat generation rate due to battery internal short-circuit ($\text{W} \times \text{m}^{-3}$)
q̇ _{abuse}	Heat generation due to thermal runaway reactions under thermal abuse conditions($\text{W} \times \text{m}^{-3}$)
Q _{Nominal}	Battery total electric capacity (Ah)
Q _{ref}	Reference capacity (Ah)—capacity of the battery used in tests
R ₁	Polarisation resistance (Ω)
R ₂	Diffusion resistance (Ω)
R _s	Ohmic resistance (Ω)
V	Volt
V ₁	Voltage across first resistor–capacitor network (V)
V ₂	Voltage across second resistor–capacitor network (V)
V _{OCV}	Open circuit voltage (V)
Vol	Active zone's volume (m^3)
C _p	Specific heat coefficient ($\text{J} \times \text{kg}^{-1} \times \text{K}^{-1}$)
T	Temperature (K)
k	Thermal conductivity ($\text{W} \times \text{m}^{-1} \times \text{K}^{-1}$)
U	Equilibrium voltage (V)
Greek letters	
σ	Effective electrical conductivity of the electrodes ($\text{S} \times \text{m}^{-1}$)
φ	Phase potential of the electrodes ($\text{V} \times \text{m}^{-1}$)
ρ	Density ($\text{kg} \times \text{m}^{-3}$)
Acronyms	
2D	Two-Dimensional
3D	Three-Dimensional
ANSYS	Analysis System

BMS	Battery Management System
CAD	Computer-Aided Design
CATIA	Computer-Aided Three-Dimension Interactive Application
CHT	Conjugate Heat Transport
C-rate	Current Charge/Discharge Rate
ECM	Equivalent Circuit Model
EV	Electric Vehicle
FEA	Finite Element Analysis
FMU	Functional Mock-up Unit
HPPC	Hybrid Power Pulse Characterisation
ICE	Internal Combustion Engine
LFP	Lithium Iron Phosphate
MATLAB	MATrix LABoratory
MSMD	Multi-Scale Multi-Domain
NEDC	New European Driving Cycle
NTGK	Newman, Tiedeman, Gu, and Kim
OCV	Open Circuit Voltage
P2D	Pseudo-Two-Dimensional
PC	Personal Computer
PTC	Positive Thermal Coefficient
RC	Resistor–Capacitor
SDO	Solve Design Optimisation
SoC	State of Charge
UDS	User-Defined Scalar
WLTP	Worldwide Harmonised Light Vehicles Test Procedure

References

1. Deng, D. Li-ion batteries: Basics, progress, and challenges. *Energy Sci. Eng.* **2015**, *3*, 385–418. [[CrossRef](#)]
2. Koech, A.K.; Mwandila, G.; Mulolani, F.; Mwaanga, P. Lithium-ion battery fundamentals and exploration of cathode materials: A review. *S. Afr. J. Chem. Eng.* **2024**, *50*, 321–339. [[CrossRef](#)]
3. BU-205: Types of Lithium-Ion-Battery University. Available online: <https://batteryuniversity.com/article/bu-205-types-of-lithium-ion> (accessed on 28 November 2023).
4. Khasawneh, H.; Neal, J.; Canova, M.; Guezenne, Y.; Wayne, R.; Taylor, J.; Smalc, M.; Norley, J. Analysis of Heat-Spreading Thermal Management Solutions for Lithium-Ion Batteries. In Proceedings of the ASME 2011 International Mechanical Engineering Congress and Exposition, IMECE 2011, Denver, CO, USA, 11–17 November 2011; pp. 421–428. [[CrossRef](#)]
5. Bandhauer, T.M.; Garimella, S.; Fuller, T.F. A Critical Review of Thermal Issues in Lithium-Ion Batteries. *J. Electrochem. Soc.* **2011**, *158*, R1. [[CrossRef](#)]
6. Saw, L.H.; Ye, Y.; Tay, A.A.O. Electrochemical-thermal analysis of 18650 Lithium Iron Phosphate cell. *Energy Convers. Manag.* **2013**, *75*, 162–174. [[CrossRef](#)]
7. Ma, S.; Jiang, M.; Tao, P.; Song, C.; Wu, J.; Wang, J.; Deng, T.; Shang, W. Temperature effect and thermal impact in lithium-ion batteries: A review. *Prog. Nat. Sci. Mater. Int.* **2018**, *28*, 653–666. [[CrossRef](#)]
8. Broatch, A.; Olmeda, P.; Margot, X.; Agizza, L. A generalized methodology for lithium-ion cells characterization and lumped electro-thermal modelling. *Appl. Therm. Eng.* **2022**, *217*, 119174. [[CrossRef](#)]
9. Srinivasan, V.; Newman, J. Discharge Model for the Lithium Iron-Phosphate Electrode. *J. Electrochem. Soc.* **2004**, *151*, A1517. [[CrossRef](#)]
10. Saw, L.H.; Ye, Y.; Tay, A.A.O. Integration issues of lithium-ion battery into electric vehicles battery pack. *J. Clean. Prod.* **2016**, *113*, 1032–1045. [[CrossRef](#)]
11. Yang, Z.; Patil, D.; Fahimi, B. Electrothermal modeling of lithium-ion batteries for electric vehicles. *IEEE Trans. Veh. Technol.* **2019**, *68*, 170–179. [[CrossRef](#)]
12. Liu, K.; Gao, Y.; Zhu, C.; Li, K.; Fei, M.; Peng, C.; Zhang, X.; Han, Q.-L. Electrochemical modeling and parameterization towards control-oriented management of lithium-ion batteries. *Control Eng. Pract.* **2022**, *124*, 105176. [[CrossRef](#)]
13. Hu, Y.; Yurkovich, S.; Guezenne, Y.; Yurkovich, B.J. Electro-thermal battery model identification for automotive applications. *J. Power Sources* **2011**, *196*, 449–457. [[CrossRef](#)]

14. Coleman, M.; Lee, C.K.; Zhu, C.; Hurley, W.G. State-of-charge determination from EMF voltage estimation: Using impedance, terminal voltage, and current for lead-acid and lithium-ion batteries. *IEEE Trans. Ind. Electron.* **2007**, *54*, 2550–2557. [CrossRef]
15. Liu, Y.; Zhang, R.; Wang, J.; Wang, Y. Current and future lithium-ion battery manufacturing. *iScience* **2021**, *24*, 102332. [CrossRef] [PubMed]
16. RS Pro Rechargeable Lithium Ion Iron Phosphate Battery (LiFePO₄). Available online: <https://uk.rs-online.com/web/p/speciality-size-rechargeable-batteries/1834305> (accessed on 18 December 2024).
17. Worldwide Harmonised Light Vehicle Test Procedure | VCA. Available online: <https://www.vehicle-certification-agency.gov.uk/fuel-consumption-co2/the-worldwide-harmonised-light-vehicle-test-procedure/> (accessed on 18 December 2024).
18. Fotouhi, A.; Proppe, K.; Auger, D.J. Electric vehicle battery model identification and state of charge estimation in real world driving cycles. In Proceedings of the 2015 7th Computer Science and Electronic Engineering Conference, CEEC 2015—Conference Proceedings, Colchester, UK, 24–25 September 2015; pp. 243–248. [CrossRef]
19. Miri, I.; Fotouhi, A.; Ewin, N. Electric vehicle energy consumption modelling and estimation—A case study. *Int. J. Energy Res.* **2021**, *45*, 501–520. [CrossRef]
20. Ansys Fluent User’s Guide. 2023. Available online: <http://www.ansys.com> (accessed on 9 March 2025).
21. Jeon, D.H.; Baek, S.M. Thermal modeling of cylindrical lithium ion battery during discharge cycle. *Energy Convers. Manag.* **2011**, *52*, 2973–2981. [CrossRef]
22. Kim, G.-H.; Smith, K.; Lee, K.-J.; Santhanagopalan, S.; Pesaran, A. Multi-Domain Modeling of Lithium-Ion Batteries Encompassing Multi-Physics in Varied Length Scales. *J. Electrochem. Soc.* **2011**, *158*, A955. [CrossRef]
23. Chen, M.; Rincón-Mora, G.A. Accurate electrical battery model capable of predicting runtime and I-V performance. *IEEE Trans. Energy Convers.* **2006**, *21*, 504–511. [CrossRef]
24. Teschner, T.-R. Lecture Notes—Grid Generation/CAD—Computational Fluid Dynamics—November 2022. 2022. Available online: www.cranfield.ac.uk (accessed on 9 March 2025).
25. Arunachala, R.; Löffler, K.; Teutsch, T.; Thanagasundram, S.; Makinejad, K.; Jossen, A. A Cell Level Model for Battery Simulation. Available online: <https://www.researchgate.net/publication/235602059> (accessed on 9 March 2025).
26. Hua, X.; Zhang, C.; Offer, G. Finding a better fit for lithium ion batteries: A simple, novel, load dependent, modified equivalent circuit model and parameterization method. *J. Power Sources* **2021**, *484*, 229117. [CrossRef]
27. Lin, X.; Perez, H.E.; Mohan, S.; Siegel, J.B.; Stefanopoulou, A.G.; Ding, Y.; Castanier, M.P. A lumped-parameter electro-thermal model for cylindrical batteries. *J. Power Sources* **2014**, *257*, 1–11. [CrossRef]
28. Estimate Equivalent Circuit Lithium-Ion Battery Data-MATLAB & Simulink-MathWorks United Kingdom. Available online: <https://uk.mathworks.com/help/autoblks/ug/estimate-equivalent-circuit-lithium-ion-battery-data.html> (accessed on 16 October 2024).
29. Lithium Battery Cell-Two RC-Branch Equivalent Circuit-MATLAB & Simulink-MathWorks United Kingdom. Available online: <https://uk.mathworks.com/help/simscape/ug/lithium-battery-cell-two-rc-branch-equivalent-circuit.html> (accessed on 16 October 2024).
30. Kim, Y.; Siegel, J.B.; Stefanopoulou, A.G. A computationally efficient thermal model of cylindrical battery cells for the estimation of radially distributed temperatures. In Proceedings of the 2013 American Control Conference, Washington, DC, USA, 17–19 June 2013; pp. 698–703. [CrossRef]
31. Ellingsen, L.A.W.; Majeau-Bettez, G.; Singh, B.; Srivastava, A.K.; Valøen, L.O.; Strømman, A.H. Life Cycle Assessment of a Lithium-Ion Battery Vehicle Pack. *J. Ind. Ecol.* **2014**, *18*, 113–124. [CrossRef]

Disclaimer/Publisher’s Note: The statements, opinions and data contained in all publications are solely those of the individual author(s) and contributor(s) and not of MDPI and/or the editor(s). MDPI and/or the editor(s) disclaim responsibility for any injury to people or property resulting from any ideas, methods, instructions or products referred to in the content.